ACS OMEGA

http://pubs.acs.org/journal/acsodf

Article

Activated Biocarbon from Paper Mill Sludge as Electrode Material for Supercapacitors: Comparative Performance Evaluation in Two Aqueous Electrolytes

Jibril Abdulsalam, Kabir Otun, Nasreen Gardee, Bilal Patel,* Taile Leswifi, and Mahlanyane Kenneth Mathe

Cite This: *ACS Omega* 2023, 8, 5285−5299

Read Online

ACCESS | Metrics & More | Article Recommendations | Supporting Information

ABSTRACT: The valorization of a South African paper mill waste sludge into an activated biocarbon electrode material for energy storage application is reported. The valorization method is a two-step synthesis that comprises hydrothermal carbonization and NaOH activation of paper mill waste at 700 °C to produce activated biocarbon. The development of high porosity carbon material with a surface area of 1139 m^2/g was observed. The synthesized biocarbon electrode exhibited good specific capacitance (C_{sp}) values of 206 and 157 Fg^{-1}, from a three-electrode cell in neutral (1 M Na_2SO_4) and alkali (3 M KOH) electrolytes, respectively. The electrolyte concentration purportedly has a considerable effect on specific capacitance. In both electrolytes, symmetric triangular curves in galvanostatic charge−discharge point to a quick charge−discharge process. Synthesized material testing with a two-electrode cell in 3 M KOH and 1 M Na_2SO_4 electrolytes, respectively, delivered specific capacitances of 125 and 152 Fg^{-1}, with the corresponding energy densities of 17.4 and 21.1 Wh kg^{-1}. The material had capacity retention efficiencies of 83 and 92% after 5000 cycles in 3 M KOH and 1 M Na_2SO_4 electrolytes, respectively. The electrode material performance of the activated biocarbon from paper sludge clearly shows its potential for electrochemical energy storage. The reported results present an exciting potential contribution of the pulp and paper industry toward the transition to green energy.

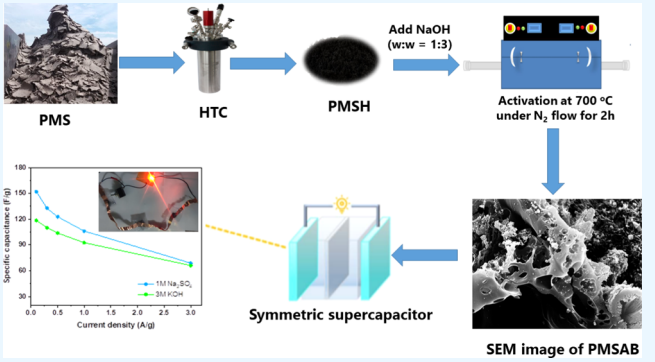

1. INTRODUCTION

Inadequate management of solid waste is a global issue. Ninety percent (90%) of South African solid waste is disposed of in landfills.[1] However, traditional disposal methods, such as landfilling and incineration, are not sustainable. Toxic landfills contain substances that subsequently seep into the soil and poison groundwater, whereas incineration is associated with the production of harmful greenhouse gases (GHGs). Thus, it is critical to develop alternative methods for managing solid waste, particularly methods capable of processing heterogeneous, high-moisture-content waste feedstock and valorizing it to provide resources that address critical energy challenges while minimizing environmental impact. Through the production of added-value products such as carbonaceous materials, the valorization of biowaste is one strategy to reduce waste, diversify income sources, and boost local economic activity, all of which contribute to a circular economy.

With the eventual depletion of fossil energy resources, an ever-increasing renewable energy uptake, and a global energy demand rise response, energy storage systems have thus become increasingly important.[2] Batteries and supercapacitors are two examples of storage devices, each with its unique advantages and drawbacks.[3,4] Although supercapacitors have a higher power density than regular batteries, they have a lower energy density (less than 10 Wh kg^{-1}).[5] Low maintenance, a rapid charge/discharge mechanism, and outstanding cyclic stability are among the advantages of supercapacitors.[6] The most significant component of a supercapacitor is electrode material since it affects its overall performance.[7] Large-scale commercial applications of supercapacitors can be achieved with a meticulous choice of electrode material and simple, low-cost preparation processes.[5] As a result, much effort is being spent in the search for low-cost novel electrode materials.

Carbonaceous materials such as activated carbons (ACs), carbon aerogels, carbon nanotubes (CNTs), carbide-derived carbons, graphene, and others have been widely used as

Received: September 11, 2022
Accepted: December 16, 2022
Published: January 31, 2023

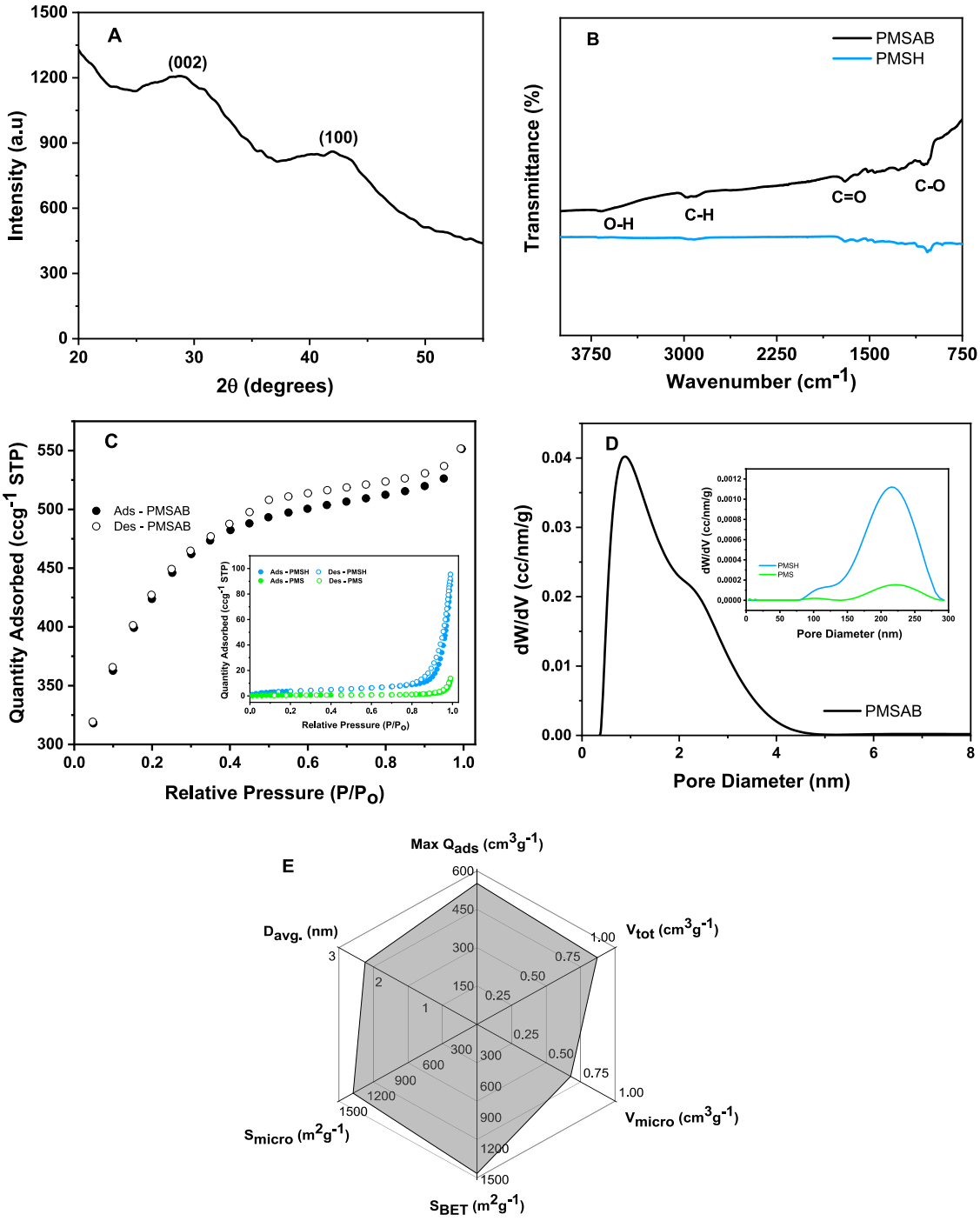

Figure 1. (A) XRD pattern of PMSAB; (B) FTIR spectra of PMSAB and PMSH; (C) N_2 isotherms of PMSAB at 77 K (the inset image shows the N_2 isotherms of PMSH and PMS); (D) pore size distribution (PSD) of PMSAB using the NLDFT method (the inset image shows the PSD of PMSH and PMS); and (E) radar chart showing the maximum quantity of nitrogen adsorbed (Q_{ads}), total pore volume (V_{tot}), micropore volume (V_{micro}), BET surface area (S_{BET}), micropore area (S_{micro}), and average pore diameter of PMSAB.

electrode materials in supercapacitors because they are cost-effective, have excellent electrical conductivity, and are widely available.[8−11] In electrochemical double-layer capacitors (EDLCs), ACs are often employed as electrode materials because of their large surface area and tunable porosity.[9] Carbon materials derived from biomass are always preferable for most applications, including gas adsorption,[12,13] wastewater treatment,[14,15] anode material in batteries,[16,17] and so on, because they are less expensive, more easily accessible, and have the least environmental impact. Biomass-derived activated carbons are gaining traction as an active electrode material for supercapacitors due to their remarkably good pore structure, ease of synthesis, high specific surface area, and high conductivity.[18]

Hydrothermal carbonization (HTC), which converts high-moisture feedstock into a carbonaceous material known as 'hydrochar', is a beneficial biomass pretreatment method. HTC eliminates the energy and cost-intensive drying process, widens raw material selection, and emits the least amount of greenhouse gases.[19−21] This procedure is carried out using

https://doi.org/10.1021/acsomega.2c05887
ACS Omega 2023, 8, 5285−5299

subcritical water at mild temperatures (180−250 °C) and autogenous pressures (2−10 MPa) for a predetermined reaction time.[22] Because of its high energy density, biomass-derived hydrochar outperforms conventional char in a variety of applications, including soil remediation, electricity generation, water purification, and as carbon electrodes in supercapacitors and batteries.[23,24] Biomass-based electrode materials in energy storage applications are seen as a promising model of green energy, sustainable development, and biomass valorization.[25,26]

Yang et al.[27] investigated the electrochemical performance of porous carbon material derived from a walnut shell in a 6M KOH electrolyte. According to the study, the material has a surface area of 724.45 m^2/g, a capacitance of 186 Fg^{-1} at a current density of 0.5 Ag^{-1}, and a capacitance retention of 100% after 20,000 cycles. The exceptional cycle performance was credited to the honeycomb-like three-dimensional morphology and the presence of oxygen-containing functional groups. Another carbon material developed from bamboo-based industrial byproducts with a specific surface area of 1472 m^2/g had a specific capacitance of 301 Fg^{-1}, an energy density of 6.1 Wh kg^{-1}, and a power density of 2.6 kW kg^{-1}.[28]

Sundriyal et al.[29] reported on the performance of activated carbons derived from pencil peel and office wastepaper as electrode materials in supercapacitors. At a current density of 1 Ag^{-1}, the carbon materials produced from pencil peel and office wastepaper had specific capacitances of 553 Fg^{-1} and 237 Fg^{-1}, respectively. The high amount of graphitic carbon in the pencil peel-derived activated carbon was cited as a reason for its superior performance. In a separate study, Sodtipinta et al.[30] used pineapple leaves to synthesize carbon nanosheets (CNS) with a surface area of 1681 m^2/g and a specific capacitance of 202 Fg^{-1}. The performance of activated carbon made from rubberwood waste by NaOH activation was reported by Thubsuang et al.[31] The carbon material was reported to have a specific surface area of 693 m^2/g and delivered an energy density of 14.2 Wh kg^{-1} and a power density of 500 W kg^{-1}.

Wang et al.[32] synthesized porous carbon materials from paper mill sludge by hydrothermal pretreatment and KOH activation, resulting in a highly porous material with a specific surface area of 2980 m^2/g. The derived carbon material was evaluated as electrode material in supercapacitors in three different organic electrolytes. The study reported specific capacitances of 162.2, 163.3, and 161.5 Fg^{-1} in TEABF4/AN, BMPY TFSI, and EMIM TFSI, respectively. In another work, porous carbon was synthesized from tea leaves using $ZnCl_2$ activation. The material with a specific surface area of 1,439.9 m^2/g exhibited a capacitance value of 256 Fg^{-1} at a current density of 0.5 Ag^{-1} in a 1 M Na_2SO_4 electrolyte.[33] There have been various other studies that have examined porous carbon materials from different biomass sources, including prawn shells,[34] sugar cane bagasse,[35] dead leaves,[36] and cotton.[37] These materials were successfully employed as electrodes in supercapacitors.

Porous carbon material from paper mill sludge has previously been examined as a supercapacitor electrode material.[32] The carbon material showed remarkable electrochemical performance in organic and ionic liquid electrolytes. However, because organic and ionic liquid electrolytes are costly, the potential of paper sludge-derived carbon material in low-cost aqueous electrolytes needs to be investigated. In contrast, organic electrolyte supercapacitor devices (SCDs) appear to be dominating the market because of their high voltage window (2.6−2.9 V). The organic electrolyte SCDs have greater resistance than aqueous electrolytes due to their large molecules, which need large-pore-size electrodes.[38] Aqueous electrolytes, on the other hand, have higher conductivity than organic and ionic electrolytes, which helps to reduce the equivalent series resistance and improve the power delivery of SCDs.[38−40]

The relationship between the structure of the carbon material, electrolyte concentration, and its electrochemical performance in aqueous electrolytes needs to be examined, as this will serve as a valuable reference for the application of paper sludge-derived porous carbon in energy storage. Hence, in this study, porous biocarbon from paper mill sludge is synthesized by first pretreating it hydrothermally and then chemically activating it with NaOH. NaOH activation plays a significant role in the creation of pores in carbon materials, which increases the material's specific surface area. Following that, the synthesized activated biocarbon (PABC) is investigated as an active electrode material for supercapacitor applications using two aqueous electrolytes: alkali (1, 3, and 6 M KOH) and neutral (0.25, 0.5, and 1 M Na_2SO_4). Finally, we conducted surface and diffusion charge contribution analyses of PABC in these electrolytes to gain a better understanding of the electrochemical charge storage mechanism of the synthesized material.

2. RESULTS AND DISCUSSION

2.1. Structural and Morphological Characterizations.

2.1.1. FTIR and XRD Characterizations. The X-ray diffraction spectrum of PMSAB, as shown in Figure 1A, revealed two broad peaks at 2θ = 28 and 41°, associated closely with (002)[41] and (100) graphitic planes, respectively.[42,43] This indicates the amorphous nature of the material and the formation of graphitic carbon structure due to the elevated temperature of the activation process. This demonstrates that hydrothermal pretreatment and NaOH activation effectively transformed PMS into an amorphous and partly graphitic carbon material. Previous studies have also reported that carbonization and activation at high temperatures have a significant impact on the development of amorphous carbon and the porous structure.[44,45]

The FTIR spectra of PMSH and PMSAB from 750 to 4000 cm^{-1} are shown in Figure 1B. The hydroxyl group produced because of chemical activation with NaOH is responsible for the O−H stretching observed for PMSAB at approximately 3547 cm^{-1}. The distinctive olefinic group responsible for the C−H stretching is noted near 2975 cm^{-1}. The difference in peak intensities for PMSH and PMSAB demonstrates the transformation that occurred during the NaOH activation process.[46]

2.1.2. Nitrogen (N_2) Adsorption Analyses. The surface characteristics determined from N_2 isotherms at 77 K for PMS, PMSH, and PMSAB are presented in Table S1. NaOH chemical activation enhanced the pore structure of PMSAB with increased micropore formation, which aids electrochemical performance.

Figure 1C shows the N_2 adsorption−desorption isotherm of PMSAB, whose profile is indicative of a type IV isotherm according to the IUPAC classification.[47] The steep increase in the lower region of the curve, just before 0.40 P/P_o, indicates the presence of micropores in the material.[48] Increased interaction between the material and nitrogen gas in the

https://doi.org/10.1021/acsomega.2c05887
ACS Omega 2023, 8, 5285−5299

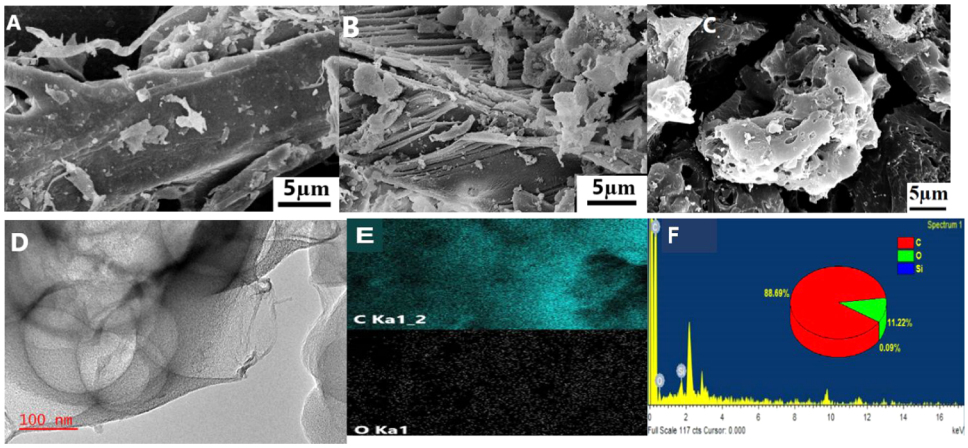

Figure 2. SEM images of (A) PMS, (B) PMSH, and (C) PMSAB; (D) TEM image of PMSAB; (E) elemental mapping images of carbon and oxygen in PMSAB; and (F) EDS spectrum and elemental composition of PMSAB.

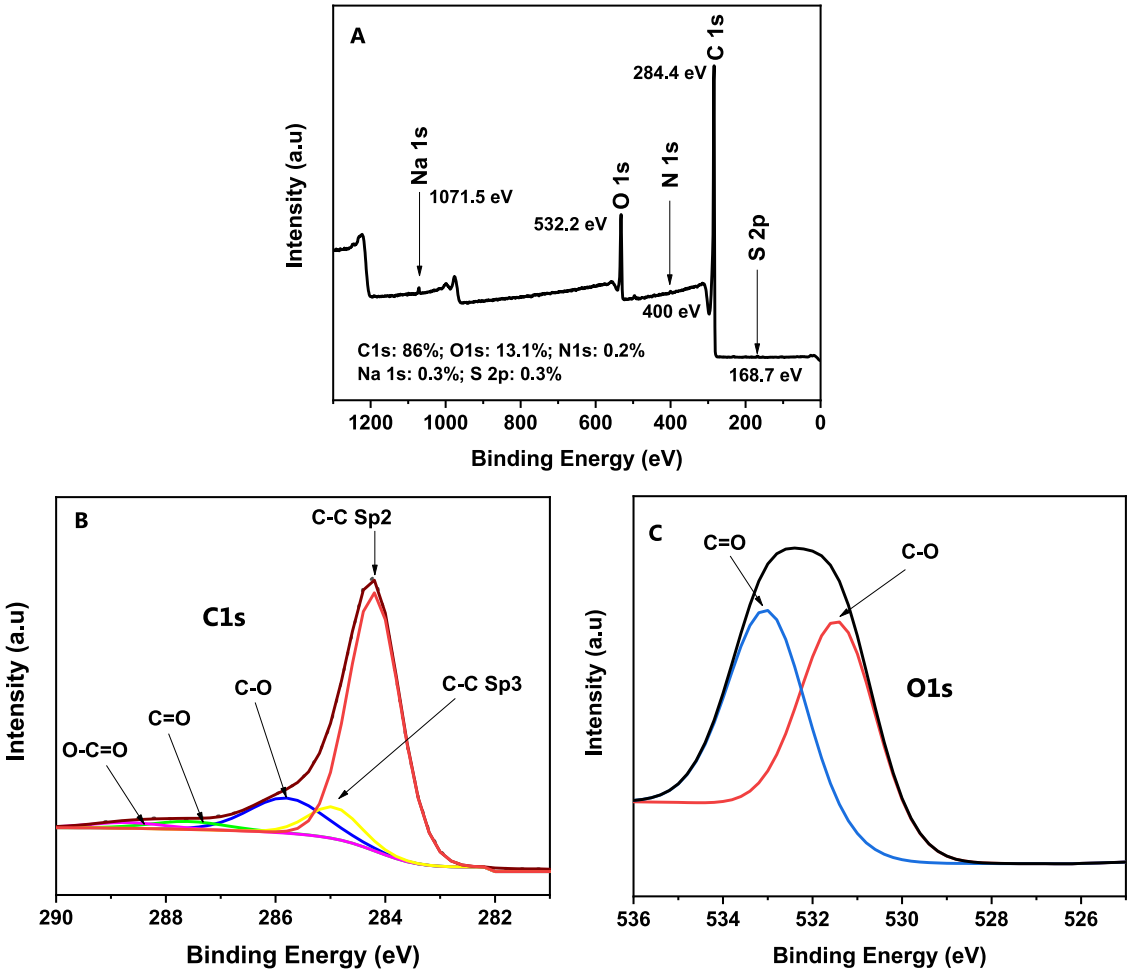

Figure 3. (A) XPS survey spectra of PMSAB and XPS spectra of (B) C 1s and (C) O 1s.

micropores ensures enhanced adsorption at low relative pressure.[49] When the relative pressure P/P_0 is greater than 0.4, the midsection of the desorption and adsorption isotherms does not overlap, resulting in a hysteresis loop. The hysteresis loop is consistent with a type IV curve having a type H3 hysteresis loop, which is an indication of the presence of mesopores in the material.[50] In electrochemical energy storage applications, microporous materials with mesopores are highly desirable as electrode materials.[5,7]

The pore size distribution (PSD) of PMSAB is shown in Figure 1D. The PSD was calculated by normalizing the pore volume to the pore width interval using the nonlocal density functional theory (NLDFT) method. The PSD peaks correspond to pore widths of 0.9 and 2.3 nm in the micropore and mesopore regions, respectively. At a pore width of around

https://doi.org/10.1021/acsomega.2c05887
ACS Omega 2023, 8, 5285−5299

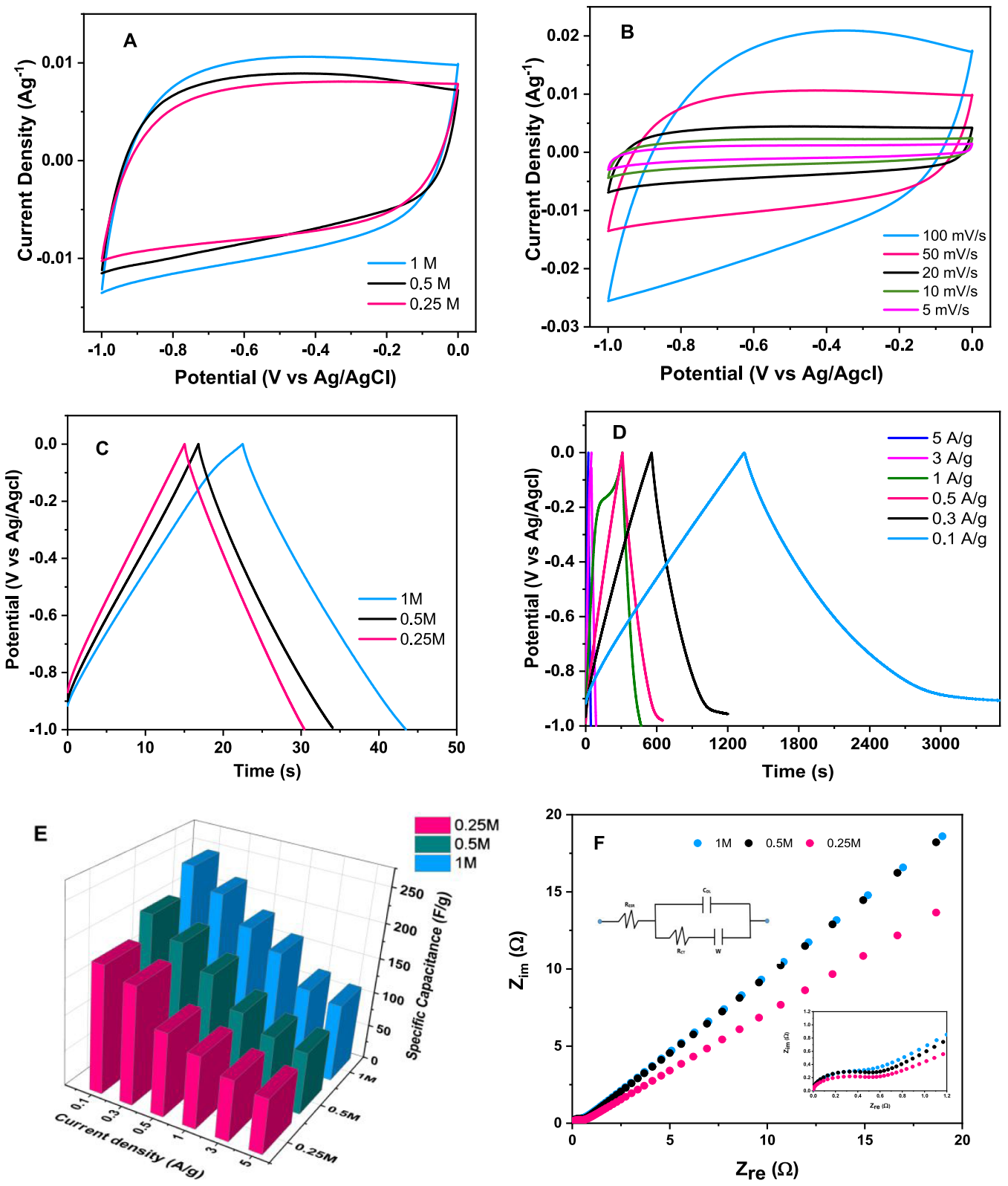

Figure 4. CV curves of (A) PMSAB in different concentrations of Na_2SO_4 electrolyte at 50 mV/s scan rates, (B) CV curves of PMSAB in 1 M Na_2SO_4 at different scan rates, (C) GCD comparison at different concentrations of Na_2SO_4 at 1 A/g, (D) GCD curves in 1 M Na_2SO_4 at different current densities, (E) specific capacitance of PMSAB as a function of current densities, and (F) Nyquist plots of PMSAB in different concentrations of Na_2SO_4 electrolyte.

4 nm, the point at which the pores are filled with nitrogen, the pore volume decreases and becomes negligible beyond the mesopore domain. The PSD curve also indicates that the material contains micropores and mesopores, making it a suitable energy storage medium. Furthermore, Figure 1E provides a radar chart depiction of the adsorptive properties of

https://doi.org/10.1021/acsomega.2c05887
ACS Omega 2023, 8, 5285−5299

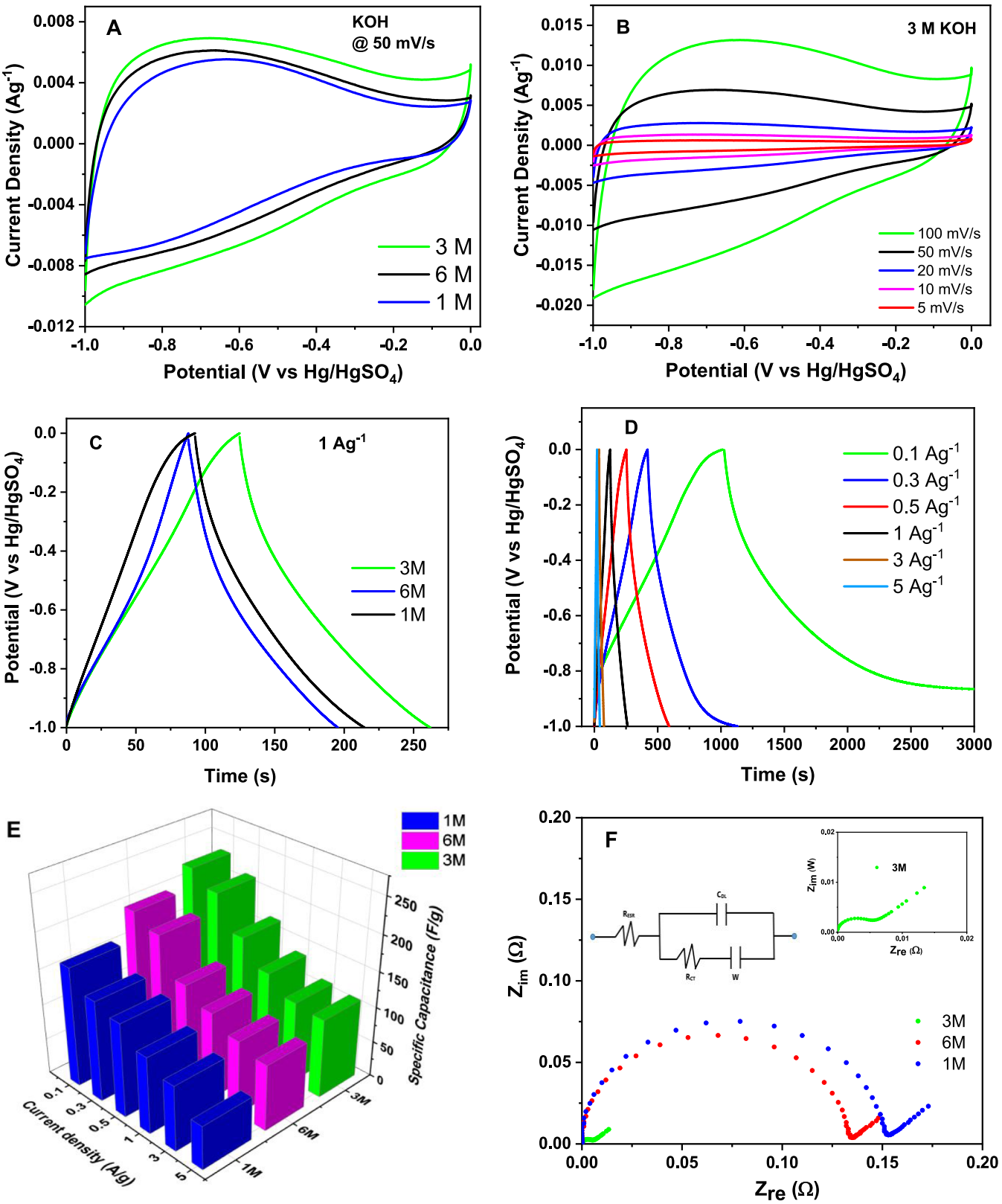

Figure 5. CV curves of (A) PMSAB in different concentrations of KOH electrolyte at 50 mV/s scan rates and (B) PMSAB in 3 M KOH at different scan rates, (C) GCD comparison in KOH with different concentrations at 1 Ag^{-1}, (D) GCD curves in 3 M KOH at different current densities, (E) specific capacitance of PMSAB as a function of current densities, and (F) Nyquist plots of PMSAB in different concentrations of KOH electrolyte.

PMSAB. The material is microporous, with micropores accounting for 78% of the total pore volume and 92% of the BET surface area, an indication that the material has a higher micropore area and volume with a marginal presence of mesopores. The micropores offer the surface area for charge storage, while the mesopores allow rapid electrolyte ion

https://doi.org/10.1021/acsomega.2c05887
ACS Omega 2023, 8, 5285−5299

adsorption and short diffusion distance, which improves the charging and discharging properties of the electrode material.[51] An electrode material must have sufficient S_{BET}, a high pore volume, and an appropriate balance between micropore and mesopore distributions for optimal performance.[20,45,46]

2.1.3. SEM/EDS and TEM Analyses. The surface morphology and porous nature of the paper sludge (PMS), hydrochar (PMSH), and activated biocarbon (PMSAB) are shown in Figure 2. The SEM image of PMS (Figure 2A) revealed a fiberlike structure. In contrast to PMS's SEM image, PMSH's SEM image (Figure 2B) exhibited a smoother surface with the formation of carbon particles while keeping the paper sludge's original fiberlike structure (PMS). This demonstrates that hydrothermal pretreatment of paper mill sludge can result in a useful carbon material. Activating the hydrochar (PMSH) with NaOH at an elevated temperature resulted in pore formation on the surface of the material, as can be seen in Figure 2C. The hydrochar underwent significant dehydrogenation and intermolecular dehydration reactions during the activation process,[52] increasing the number of pores on the surface of the activated material. The TEM images of PMSAB, as shown in Figure 2D, show an amorphous structure and reveal a nanosheet layer structure with multiple arrays of pores that overlap each other.[53]

The elemental mapping images and compositions for PMSAB as determined by EDS are shown in Figure 2E,F. The distribution of C and O is detected according to EDS mapping. The homogeneous distribution showed that the hydrothermal pretreatment and subsequent activation were effective and reacted uniformly throughout the material's surface.

2.1.4. XPS Analyses. The PMSAB XPS survey spectra in Figure 3A demonstrate the coexistence of carbon (C), oxygen (O), and nitrogen (N), and the fitting result reveals that PMSAB is mostly constituted of C (88.5%), O (10.8%), and N (0.3%). These numbers match those obtained from the EDS spectra. C−C Sp3 (284.2 eV), C−C Sp2 (284.9 eV), C−O (285.8 eV), C═O (287.6 eV), and O−C═O (288.7 eV) are the five different peaks in the C 1s spectra (Figure 3B).[54] The O 1s spectra (Figure 3C) show two peaks at 531.4 and 533 eV, corresponding to C−O and C═O, respectively.[55] The PMSAB survey scan revealed the presence of sodium, nitrogen, and sulfur on the surface of the sample. The Na 1s peak is at 1071.5 eV, the N 1s peak is at 399.8 eV, and the S 2p peak is at 168.7 eV. The Na on the surface is likely to be derived from the NaOH used in the activation process. The N 1s peak is attributable to organic nitrogen molecules, such as amide and amine.[56] The peak (S 2p) at a binding energy of 168.2 eV represents SO_2.[57]

2.2. Electrochemical Evaluation of PMSAB as Electrode Material. *2.2.1. CV, GCD, and EIS Analyses in Na_2SO_4 Electrolyte.* The CV curves of PMSAB at 50 mV/s in Na_2SO_4 electrolyte at different concentrations of 0.25, 0.5, and 1 M are shown in Figure 4A. At varying concentrations, the symmetrical rectangular form of the PMSAB electrode indicates an EDLC-type supercapacitor. The CV curve of the electrode has sharper edges and a larger area at 1 M concentration compared to other concentrations. This demonstrates that the material's capacitance is greater in 1 M Na_2SO_4 electrolyte than those at 0.25 and 0.5 M concentrations. The performance of PMSAB in 1 M Na_2SO_4 electrolyte at scan rates of 5−100 mV/s is shown in Figure 4B. Increased scan rates might lead to an increase in the internal resistance between the electrolyte and the electrode material's pore wall.[58,59] With increasing scan rates, these internal resistances may induce progressive distortion of CV curves, resulting in lower specific capacitance.[60,61]

Figure 4C depicts the GCD curves of the material at 1 Ag^{-1} current density in different concentrations (0.25, 0.5, and 1 M) of Na_2SO_4 electrolyte. The material in Na_2SO_4 electrolyte exhibits symmetric charge−discharge curves at varied concentrations, indicating an EDLC-type supercapacitor. The material has a longer discharge duration at 1 M concentration, which might be due to the increase in salt concentration of the electrolyte, which would increase the dominance of free ions and ionic conductivity and, in turn, enhance charge storage.[38,62] The specific capacitance of the material was determined using eqs 1 and 2 and the GCD curves at various Na_2SO_4 concentrations. The specific capacitances of PMSAB at concentrations of 0.25, 0.5, and 1 M and 1 Ag^{-1} are 95, 106, and 137 Fg^{-1}, respectively.

Figure 4D shows the GCD curves obtained from increasing current densities of PMSAB in 1 M Na_2SO_4 electrolyte. When the current density was increased from 0.1, 0.3, 0.5, 1, 3, and 5 Ag^{-1}, the specific capacitance decreased steadily from 206, 173, 158, 137, 122, and 118 Fg^{-1}, respectively. This decrease in specific capacitance as the current density increases could be attributed to the fact that higher current density limits the maximum utilization of the pores of the material, thereby contributing to the surge in internal resistance.[63] Electrolyte diffusion through micro- and mesopores promotes electrochemical activity at low charging rates, leading to a significant increase in specific capacitance. However, at high charging rates, the electrolyte can only access a limited number of mesopores, resulting in a considerable reduction in specific capacitance.[64] As shown in Figure 4E, the specific capacitance of the material at 0.5 and 0.25 M concentrations followed a similar capacitance trend as the current density increased. For comparison, the specific capacitance values at all current densities are tabulated in Table S2 in the Supplementary Information.

Figure 4F displays the Nyquist plots of PMSAB in varied concentrations of Na_2SO_4 electrolyte. The curves' semicircle represents internal resistance, which is the sum of bulk electrolyte resistance and charge-transfer resistance.[60] In addition, the capacitive behavior of the electrode is shown by slanted straight lines toward the lower-frequency region.[63]

2.2.2. CV, GCD, and EIS Analyses in KOH Electrolyte. The electrochemical performance of PMSAB was examined in various concentrations (1, 3, and 6 M) of KOH electrolyte. The CV curves at various scan rates (5−100 mV/s) are shown in Figure 5A,B. The CV curve of the material in various concentrations of KOH shows a quasi-rectangular shape, indicating a capacitive response contributed by EDLC and a relatively small internal resistance.[65]Figure 5C,D shows the GCD curves of PMSAB at current densities of 0.1 and 5 Ag^{-1} in different KOH concentrations, respectively. The curves are perfectly symmetric. PMSAB has a maximum capacitance of 157 Fg^{-1} at 0.1 Ag^{-1} and 3 M concentration. The specific capacitance values at all current densities are tabulated in Table S3.

In general, like the pattern reported with Na_2SO_4 electrolyte, at low charging rates, electrolyte diffusion through the porous surface of the material enhances electrochemical activity, hence increasing specific capacitance. However, at high charging rates, the electrolyte can only access a limited number of pores,

https://doi.org/10.1021/acsomega.2c05887
ACS Omega 2023, 8, 5285−5299

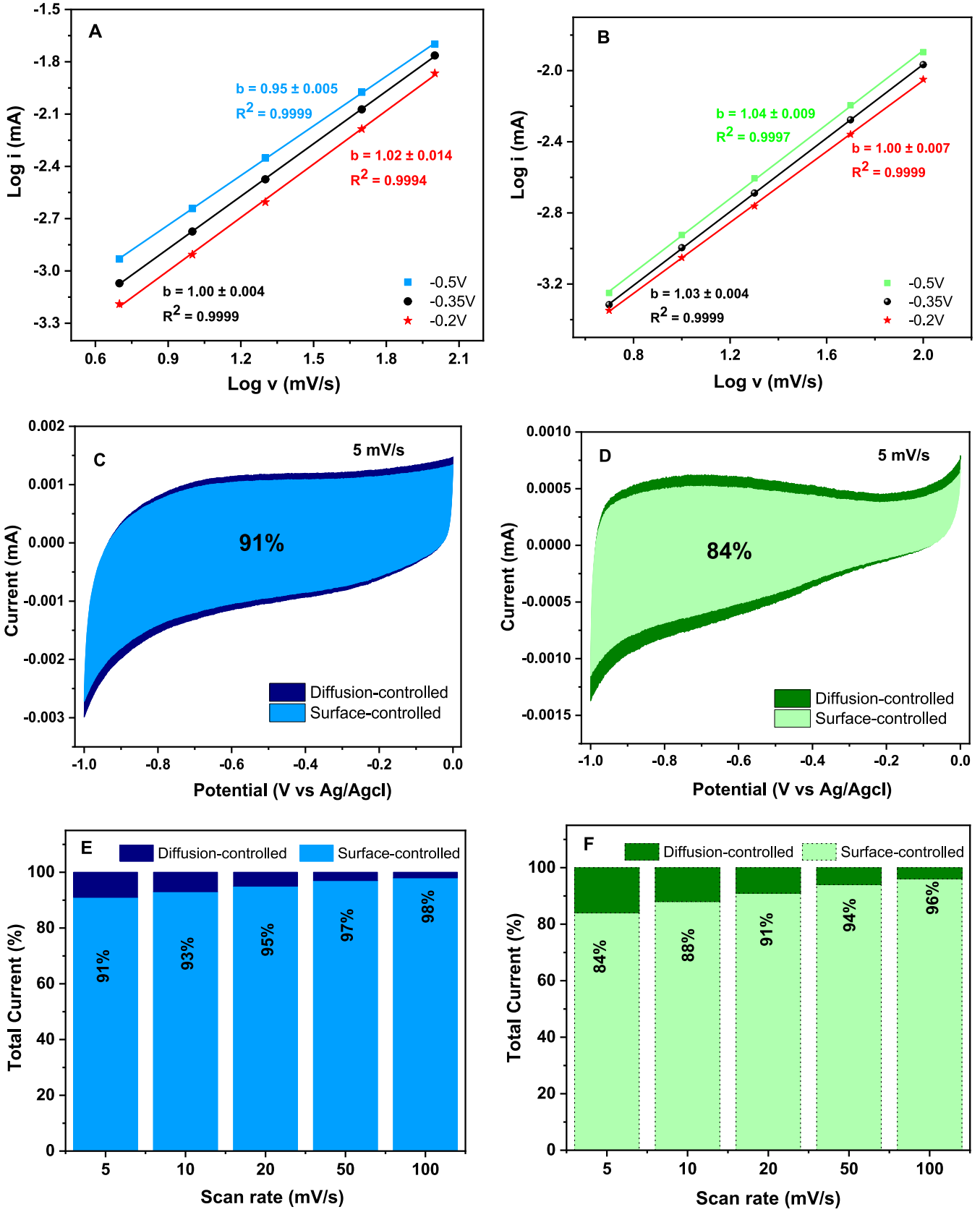

Figure 6. Log peak current vs log scan rate for PMSAB in (A) 1 M Na_2SO_4 and (B) 3 M KOH obtained at the cathodic directions; contribution of charge storage from the surface and diffusion-controlled mechanism from CV at 5 mV/s for (C) 1 M Na_2SO_4 and (D) 3 M KOH, and histograms of the percentage charge storage contributions from the surface and diffusion-controlled mechanism from 5 to 100 mV/s for (E) 1 M Na_2SO_4 and (F) 3 M KOH.

https://doi.org/10.1021/acsomega.2c05887
ACS Omega 2023, 8, 5285−5299

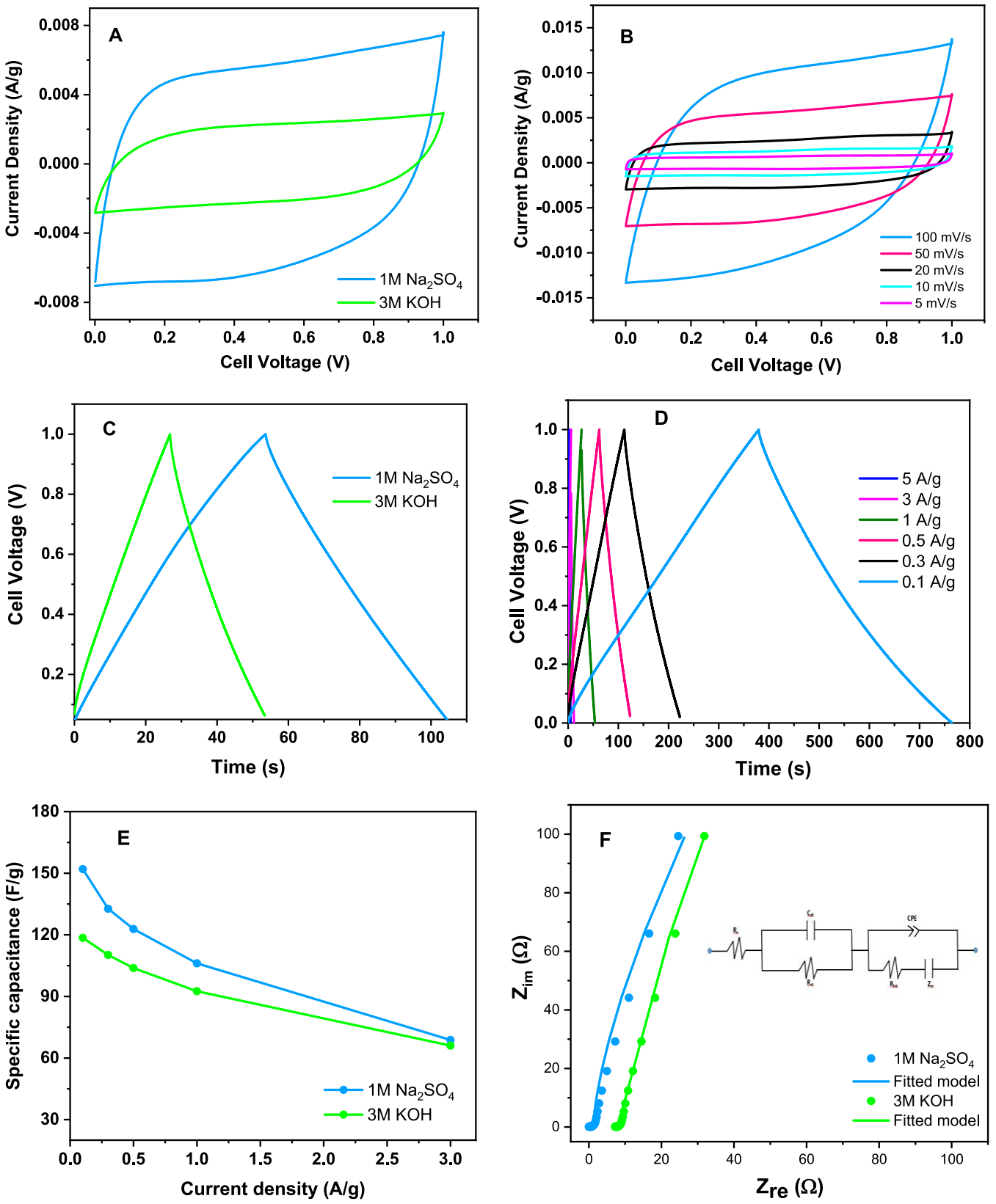

Figure 7. (A) CV curves of PMSAB in 1 M Na_2SO_4 and 3 M KOH at 50 mV/s scan rate, (B) CV curves of PMSAB in 1 M Na_2SO_4 at different scan rates, (C) GCD comparison of PMSAB in 1 M Na_2SO_4 and 3 M KOH at 1 A/g, (D) GCD curves of PMSAB in 1 M Na_2SO_4 at different current densities, (E) comparison of specific capacitance at different current densities, and (F) Nyquist plots of the two-electrode cell (symmetric) with PMSAB in 1 M Na_2SO_4 and 3 M KOH electrolytes.

resulting in a considerable reduction in specific capacitance, as shown in Figure 5E.

The resulting Nyquist plot from the EIS analysis was fitted using an equivalent circuit model (Figure 5F) that included

https://doi.org/10.1021/acsomega.2c05887
ACS Omega 2023, 8, 5285−5299

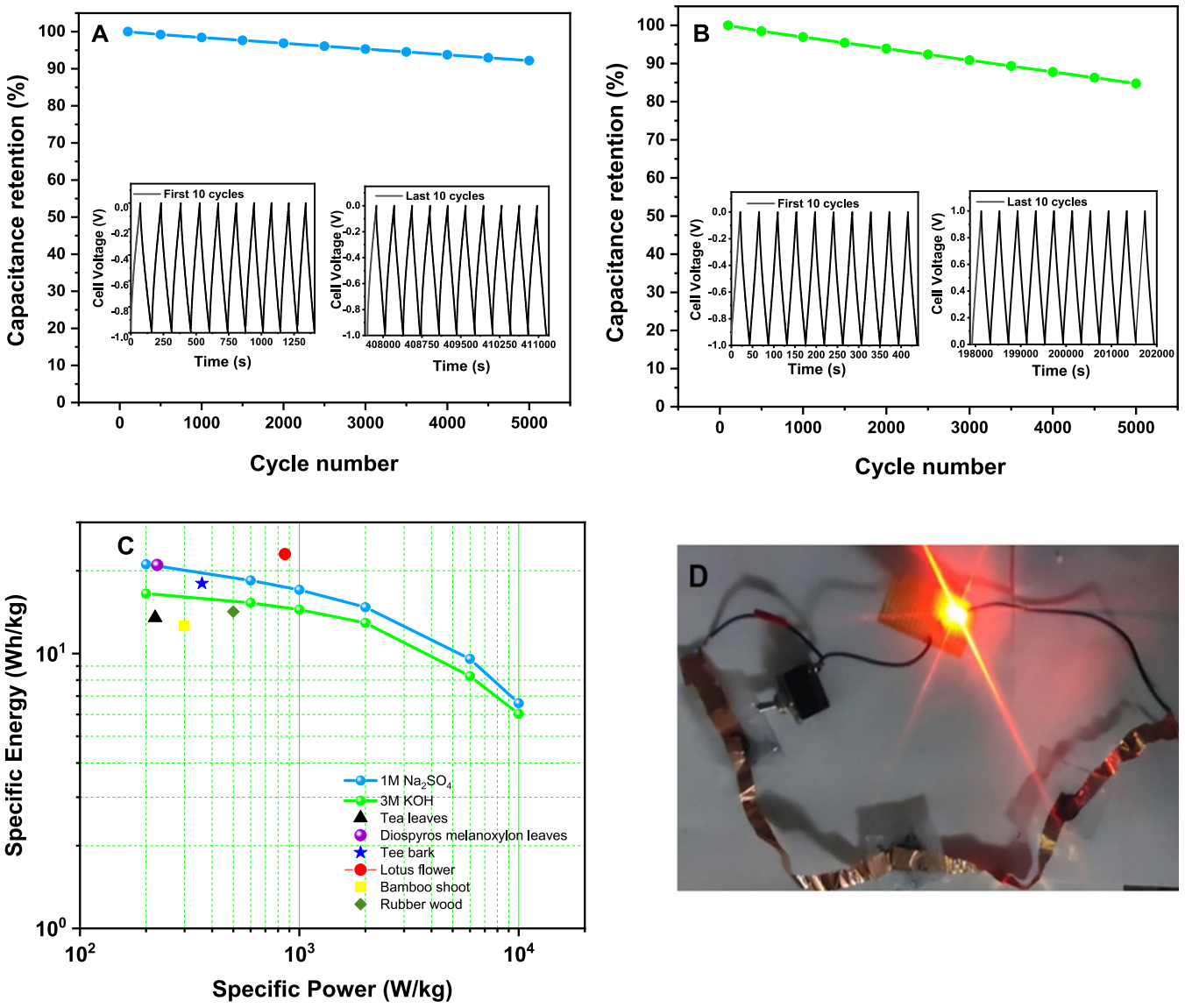

Figure 8. (A) Capacitance retention of PMSAB in 1 M Na_2SO_4 up to 5000 cycles, (B) capacitance retention of PMSAB in 3 M KOH up to 5000 cycles, (C) Ragone plot for the PMSAB symmetric cell in Na_2SO_4 and KOH electrolytes, and (D) 2 V LED bulb illuminated by three PMSAB symmetric cells in 1 M Na_2SO_4 connected in series.

physical components such as solution resistance (R_s), charge-transfer resistance (R_{ct}), and double-layer capacitance (C_{dl}). The plot demonstrated that the lowest internal resistance, which is the sum of R_s and R_{ct}, is found in 3 M KOH. The ascending slope that occurs in the low-frequency range reveals the PMSAB electrode material's capacitive behavior.

2.2.3. Electrochemical Kinetic Analyses. The electrochemical kinetic analysis was conducted to further probe the charge storage mechanisms between the two electrolytes (KOH and Na_2SO_4). To achieve that, eqs 6 and 7 were used to ascertain the surface- and diffusion-controlled mechanism from the CV data of PMSAB in both electrolytes (1 M Na_2SO_4 and 3 M KOH). The intercept of the *y*-axis (b) from the plot of log(i) vs log(v) describes the charge storage mechanism. The *b*-values of the PMSAB in both electrolytes were obtained from the slopes of the plots of log(i) vs against log(v), as shown in Figure 6A,B. The value of b = 1 indicates a charge storage process dominated by a surface-controlled mechanism, while b = 0.5 indicates that the process is diffusion-controlled. The value of b between 0.5 and 1 is an indication of a combined mechanism. It is, therefore, necessary to evaluate the percentage contribution of each of the mechanisms in the storage process.

The current contribution from capacitive and diffusion effects was computed based on the CV curves obtained at various scan rates using eq 8. A plot of $I(V)/v^{1/2}$ and $v^{1/2}$ will give a slope of k_1 and intercept, k_2. The fraction of capacitive contribution increases with the scan rate as compared to the diffusive-controlled process, which decreases with the scan rate. This implies that a capacitive process as expected of EDLC-type material dominates the storage mechanism. Interestingly, the material (PMSAB) in the 3 M KOH electrolyte displays different electrochemical kinetics from the same material in the 1 M Na_2SO_4 electrolyte solution. At 5 mV/s, the capacitive process contributed to the total capacitance by 84 and 91% for KOH and Na_2SO_4 electrolytes, respectively (Figure 6C,D). The capacitive contribution from KOH increased from 84% at 5 mV/s to 96% at 100 mV/s,

https://doi.org/10.1021/acsomega.2c05887
ACS Omega 2023, 8, 5285−5299

while that of Na_2SO_4 increased from 91% at 5 mV/s to 98% at 100 mV/s (Figure 6E,F). In addition, the values of k_1 and k_2 in the Na_2SO_4 electrolyte are both greater than the values in the KOH electrolyte at low potentials. The high percentage of capacitive contribution further justified the outstanding rate performance of PMSAB in 1 M Na_2SO_4, indicating that the material possesses a fast redox reaction during the electrochemical process.

2.2.4. CV, GCD, and EIS Analyses in a Two-Electrode System. The potential use of PMSAB in electrochemical supercapacitors was investigated using a two-electrode symmetric setup. Figure 7A shows the CV profile of the PMSAB electrode in a symmetric cell at a scan rate of 50 mV/s in 1 M Na_2SO_4 and 3 M KOH electrolytes. Figure 7B shows the CV curves of the PMSAB electrode at various scan rates in 1 M Na_2SO_4 electrolyte. The CV curve of the PMSAB electrode was found to have a rectangular shape, which is typical of an EDLC-type supercapacitor. The shape of the CV curves demonstrated that the PMSAB electrode has high capacitive performance in both aqueous electrolytes, and the similar rectangular shape at varying scan rates shows good stability for charge storage.

Figure 7C depicts the GCD profile of the PMSAB electrode in 1 M Na_2SO_4 and 3 M KOH at a current density of 1 Ag^{-1}, whereas Figure 7D depicts the GCD curve of PMSAB in 1 M Na_2SO_4 at various current densities. The charging behavior was nearly linear and symmetrical to the discharging behavior, indicating that PMSAB has a good reversible reaction and high current efficiency.[66] The specific capacitance (C_{sp}) of the material in a two-electrode setup from the GCD curves was obtained using eq 3. The C_{sp} values of PMSAB in 3 M KOH were 125, 114, and 110 Fg^{-1} at currents of 0.1, 0.3, and 0.5 Ag^{-1}, respectively. The corresponding C_{sp} values of PMSAB in 1 M Na_2SO_4 were 152, 137, and 128 Fg^{-1} at the same current densities. With increased current density, the C_{sp} decreased (Figure 7E). This is because the Na_2SO_4 or KOH electrolyte ion has limited access to the PMSAB electrode pores at higher current densities.[67]

To understand the various resistances of the two-electrode systems in alkali and neutral electrolytes, EIS studies were conducted at a frequency range of 100 kHz to 10 mHz. Figure 7F depicts the Nyquist plots of the full cell (symmetric) fabricated with PMSAB in 1 M Na_2SO_4 and 3 M KOH aqueous electrolytes. A Voigt electrical equivalent circuit was used to fit the curves (Figure 8F, inset). Physical components such as solution resistance (R_s), charge-transfer resistance (R_{ct}), and double-layer capacitance (C_{dl}) are shown by the fitted model. The numerical values obtained from the fitted profile showed that the R_s and R_{ct} of the cell with 1 M Na_2SO_4 are lower (7.9 and 0.0012 Ω, respectively) than the R_s and R_{ct} of the cell with 3 M KOH electrolyte, which are 13.9 and 2 Ω, respectively. The material's ideal capacitive behavior is shown by the vertical slope in the low-frequency region.

The cyclic stability of the PMSAB electrodes was examined at 2.32 and 0.8 mA currents in 3 M KOH and 1 M Na_2SO_4 aqueous electrolytes, respectively. Figure 8A,B shows the percentage of PMSAB electrode capacitance retention as a function of cycle number. After 5000 cycles in 3 M KOH and 1 M Na_2SO_4 electrolytes, the results showed capacitive retention values of 82 and 92%, respectively. The electrochemical stability is determined not only by the composition of the electrolytes but also by how well they interact with the electrodes.[38] The material's higher capacitive retention in 1 M Na_2SO_4 indicates that it is more compatible with the neutral electrolyte than the alkali electrolyte, resulting in superior stability and reusability. For clarity and conciseness, Table S4 summarizes the key performance parameters for PMSAB in both electrolytes.

Figure 8C compares the energy and power density of PMSAB in Na_2SO_4 and KOH electrolytes with those of other biomass-derived porous materials employed in supercapacitor applications. The fabricated symmetric full cell has energy densities of 21.1 and 17.4 Wh kg^{-1} at a power density of 200 W kg^{-1} in 1 M Na_2SO_4 and 3 M KOH, respectively. These values exceed some reported energy densities of biomass-based carbon symmetrical supercapacitors in aqueous electrolytes, such as those made from tea leaves (13.5 Wh kg^{-1}, 220 W kg^{-1}),[33] bamboo shoot (12.6 Wh kg^{-1}, 299 W kg^{-1}),[68] and rubberwood (14.2 Wh kg^{-1}, 500 W kg^{-1}).[31] The Ragone plots of these carbon symmetrical supercapacitors made from biomass are compared and displayed in Figure 8C. Table S5 provides a comparison of biomass carbon sources, activation methods, electrolytes, and supercapacitor performance with PMSAB. The low internal resistance and high specific capacitance of PMSAB at varied current densities are responsible for its high energy and power density in both electrolytes. PMSAB has a well-defined micropore and mesopore structure and a large surface area, which results in good electrochemical performance and long-term cyclic stability. When three PMSAB symmetrical cells in 1 M Na_2SO_4 are connected in series, the PMSAB electrode light up a 2 V LED, as shown in Figure 8D. When charged to 3 V for 45 s, the light stayed on for more than 3 min.

3. CONCLUSIONS

This study presents a process for producing a biomass-based electrode using porous carbon material (PMSAB) from paper mill sludge for use in supercapacitors. The performances of a PMSAB-based supercapacitor successfully fabricated in three-electrode and two-electrode cells were evaluated in neutral (Na_2SO_4) and alkali (KOH) electrolytes. The PMSAB electrodes demonstrated satisfactory capacitive performance and good cyclic stability. The PMSAB electrode demonstrated double-layer behavior, a linear symmetrical triangle charge−discharge curve, and high cycle performance in full-cell symmetric studies. The PMSAB electrode has superior electrochemical performance in 1 M Na_2SO_4, with a specific capacitance of 152 Fg^{-1} compared to 125 Fg^{-1} in a 3 M KOH electrolyte. A GCD study also produced symmetrical triangular curves that explained the rapid charge−discharge process. Following 5000 cycles in 1 M Na_2SO_4 and 3 M KOH, the respective capacitance retention stabilized at 92 and 83%, respectively. PMSAB has a well-defined porous structure and high surface area, contributing to its promising electrochemical performance. Paper mill sludge, as an electrode material source for supercapacitors, might thus be considered promising. Future studies may consider heteroatom doping of PMSAB. Doping carbon materials with heteroatoms has been proven to be an efficient way to improve electrochemical performance by increasing electrical conductivity, providing more pseudocapacitance, and widening the operating potential window.

4. EXPERIMENTAL SECTION

4.1. Hydrothermal Pretreatment. Hydrothermal pretreatment (carbonization) was conducted in a 100 mL Berghof

https://doi.org/10.1021/acsomega.2c05887
ACS Omega 2023, 8, 5285−5299

pressure reactor. About 60 g of paper mill sludge (PMS) and 240 mL of distilled water were added to the reactor. The reaction parameters were a temperature of 250 °C and a reaction time of 90 min. At the end of the reaction time, the reactor was cooled to ambient temperature. Subsequently, the pretreated product was filtered to separate the solid from the liquid. The solid part (paper mill sludge hydrochar, PMSH) was oven-dried overnight at 105 °C.

4.2. Synthesis of Activated Biocarbon (PMSAB). The activation behaviors and, consequently, the adsorption capabilities of carbon materials are primarily determined by the nature of carbon precursors, their intrinsic reactivity, and their structural order. NaOH had been reported to be a much more effective activating hydroxide for less ordered lignocellulosic materials.[69] Hence, the hydrochar (PMSH) was physically mixed with sodium hydroxide (NaOH) in a weight ratio of 1:3. The mixture was then heated to 700 °C in a tube furnace under nitrogen gas flow. The heating rate was set to 5 °C/min, with a 3 h hold time at the desired temperature of 700 °C. After activation, the material was allowed to cool to ambient temperature under nitrogen gas flow. The sample was then washed with 1 M HCl and distilled water and dried overnight at 105 °C to obtain the paper mill sludge-activated biocarbon (PMSAB).

4.3. Material Characterizations. A Carl Zeiss Sigma field emission scanning electron microscope (SEM) coupled with an Oxford X-act EDS detector was used to study the elemental composition and morphology of the material. Transmission electron microscopy (TEM) analysis was conducted using an FEI Tecnai T12 at an accelerating voltage of 120 kV. X-ray photoelectron spectroscopy (XPS) analysis was conducted with a Thermo ESCAlab 250Xi. X-ray diffraction (XRD) analysis was conducted with a Bruker D2 PHASER Meas Srv D2-208365 with an SSD 160 operating at 30 kV and 10 mA. Fourier transform infrared (FTIR) spectra were determined using a PerkinElmer Spectrum 2 FTIR spectrometer. A surface area and porosity analyzer (Micromeritics Tristar) was used to extract nitrogen (N_2) adsorption and desorption isotherms at 77 K and other textural parameters. Before the analysis, the sample was degassed at 200 °C for 12 h. The nonlocal density functional theory (NLDFT) method[70] was used to calculate the pore size distribution using N_2 adsorption data and an assumption of carbon with slit-pore geometry.

4.4. Electrochemical Characterizations. The electrochemical characteristics of PMSAB as an electrode material were initially measured in a three-electrode system (half-cell) and then in a two-electrode system (full-cell). PMSAB was mixed with carbon black and PTFE in an 8:1:1 ratio to make the electrode. The resulting slurry was coated on a nickel foam and oven-dried overnight at 105 °C. The Ni foam was sonicated in a 1 M HCl solution for 30 min, rinsed several times with distilled water, and dried before use. The average mass loading was 2−2.3 mg/cm^2. The coated nickel foam worked as the working electrode, the platinum wire worked as the counter electrode, and Ag/AgCl worked as the reference electrode in the three-electrode configuration. The coated nickel foam was punched into 5 mm circular discs for the two-electrode setup. Stainless steel (Swagelok) fittings were used to assemble two symmetric electrode cells, with a 7 mm diameter glass-fiber filter paper (Whatman) serving as the separator (Figure S1).

A Gamry 1010E potentiostat was used for the electrochemical investigations, which include cyclic voltammetry (CV), galvanostatic charge−discharge (GCD), and electrochemical impedance spectroscopy (EIS). All analyses were conducted in varying concentrations of potassium hydroxide (KOH) and sodium sulfate (Na_2SO_4) electrolytes. The following equations were used to compute the specific capacitance (C_{sp}), energy density (E), and power density (P) based on the discharge time from GCD curves. The capacitance (C) was computed from eq 1 as follows

$$C = \frac{I \times \Delta t}{\Delta V} \tag{1}$$

Equation 1 applies when a supercapacitor's GCD curve is linear. However, when the GCD curves are nonlinear, eq 2 applies, where the capacitance is calculated by integrating the areas under the charge and discharge parts of the GCD curve.

$$C = I \int (1/V(t))\mathrm{d}t \tag{2}$$

where C is the capacitance in F, I is the current in A, Δt is the discharge time in s, and V is the potential.

The specific capacitance (C_{sp}) for a three-electrode configuration is calculated as follows

$$C_{sp} = \frac{C}{m} \tag{3}$$

where m is the mass of PMSAB in g.

For a two-electrode configuration, the specific capacitance is calculated as follows

$$C_{sp} = \frac{4C}{m} \tag{4}$$

In this case of a symmetric cell, m is the total mass of the working and counter electrode.

The energy density (E) in Wh kg^{-1} is calculated from eq 5

$$E = \frac{C \times (\Delta V)^2}{2m} \times \frac{1000}{3600} \tag{5}$$

The power density (P) in W kg^{-1} is calculated from eq 6

$$P = \frac{E \times 3600}{\Delta t} \tag{6}$$

4.5. Electrochemical Kinetics. The following equations[71] were used to evaluate the charge storage mechanisms in the two electrolytes (3 M KOH and 1 M Na_2SO_4).

$$i = a\nu^b \tag{7}$$

$$\log i = b \log \nu + \log a \tag{8}$$

where i is the current density and a and b are the parameters obtained from the slope and intercept of a plot of $\log(i)$ vs $\log(\nu)$.

The current contribution from capacitive and diffusion effects was evaluated using the following equations

$$I(V) = k_1\nu + k_2\nu^{1/2} \tag{9}$$

where $I(V)$ is the current under fixed voltage and k_1 and k_2 are the constants corresponding to capacitive- and diffusion-controlled processes, respectively.

https://doi.org/10.1021/acsomega.2c05887
ACS Omega 2023, 8, 5285−5299

■ ASSOCIATED CONTENT

Supporting Information

The Supporting Information is available free of charge at https://pubs.acs.org/doi/10.1021/acsomega.2c05887.

Schematic of a symmetric two-electrode stainless steel (Swagelok) electrochemical double-layer capacitor, textural characteristics of PMSAB from N_2 isotherms at 77 K, PMSAB specific capacitance in various concentrations of Na_2SO_4 electrolyte in a three-electrode cell configuration, PMSAB specific capacitance in various concentrations of KOH electrolyte in a three-electrode cell configuration, summary of the key performance parameters, and comparison of electrochemical performance of PMSAB with other biomass-derived porous carbons reported in the literature (PDF)

■ AUTHOR INFORMATION

Corresponding Author

Bilal Patel − *Department of Chemical Engineering, University of South Africa, Johannesburg 1709, South Africa;* orcid.org/0000-0002-1681-0249; Phone: +27 (0) 11 471 2829; Email: patelb@unisa.ac.za

Authors

Jibril Abdulsalam − *Department of Chemical Engineering, University of South Africa, Johannesburg 1709, South Africa*

Kabir Otun − *Institute for the Development of Energy for African Sustainability, University of South Africa, Johannesburg 1709, South Africa*

Nasreen Gardee − *Department of Chemical Engineering, University of South Africa, Johannesburg 1709, South Africa*

Taile Leswifi − *Department of Chemical Engineering, University of South Africa, Johannesburg 1709, South Africa*

Mahlanyane Kenneth Mathe − *Department of Chemistry, University of South Africa, Johannesburg 1709, South Africa*

Complete contact information is available at: https://pubs.acs.org/10.1021/acsomega.2c05887

Notes

The authors declare no competing financial interest.

■ ACKNOWLEDGMENTS

This study was supported and funded by the PAMDEV NPC and the Department of Science and Innovation (DSI).

■ REFERENCES

(1) Godfrey, L. K.Finding Value in Waste: Identifying Opportunities for Growth in A Secondary Resources Economy, 2015, www.researchspace.csir.co.za.

(2) Wang, Z.-L.; Guo, R.; Li, G.-R.; Lu, H.-L.; Liu, Z.-Q.; Xiao, F.-M.; Zhang, M.; Tong, Y.-X. Polyaniline nanotube arrays as high-performance flexible electrodes for electrochemical energy storage devices. *J. Mater. Chem.* **2012**, *22*, 2401−2404.

(3) Yang, L.-Y.; Cao, J.-H.; Cai, B.-R.; Liang, T.; Wu, D.-Y. Electrospun MOF/PAN composite separator with superior electrochemical performances for high energy density lithium batteries. *Electrochim. Acta* **2021**, *382*, No. 138346.

(4) Simon, P.; Gogotsi, Y.; Dunn, B. Where do batteries end and supercapacitors begin? *Science* **2014**, *343*, 1210−1211.

(5) Ghosh, S.; Santhosh, R.; Jeniffer, S.; Raghavan, V.; Jacob, G.; Nanaji, K.; Kollu, P.; Jeong, S. K.; Grace, A. N. Natural biomass derived hard carbon and activated carbons as electrochemical supercapacitor electrodes. *Sci. Rep.* **2019**, *9*, No. 16315.

(6) Hsieh, C.-T.; Chen, Y.-C.; Chen, Y.-F.; Huq, M. M.; Chen, P.-Y.; Jang, B.-S. Microwave synthesis of titania-coated carbon nanotube composites for electrochemical capacitors. *J. Power Sources* **2014**, *269*, 526−533.

(7) Yao, F.; Pham, D. T.; Lee, Y. H. Carbon-based materials for lithium-ion batteries, electrochemical capacitors, and their hybrid devices. *ChemSusChem* **2015**, *8*, 2284−2311.

(8) Zhang, X.; Zhang, H.; Lin, Z.; Yu, M.; Lu, X.; Tong, Y. Recent advances and challenges of stretchable supercapacitors based on carbon materials. *Sci. China Mater.* **2016**, *59*, 475−494.

(9) Dubey, R.; Guruviah, V. Review of carbon-based electrode materials for supercapacitor energy storage. *Ionics* **2019**, *25*, 1419−1445.

(10) Bortamuly, R.; Naresh, V.; Das, M. R.; Kumar, V. K.; Muduli, S.; Martha, S. K.; Saikia, P. Titania supported bio-derived activated carbon as an electrode material for high-performance supercapacitors. *J. Energy Storage* **2021**, *42*, No. 103144.

(11) Zhou, J.; Zhang, S.; Zhou, Y.-N.; Tang, W.; Yang, J.; Peng, C.; Guo, Z. Biomass-derived carbon materials for high-performance supercapacitors: current status and perspective. *Electrochem. Energy Rev.* **2021**, *4*, 219−248.

(12) Asgarpour Khansary, M.; Aroon, M. A.; Shirazian, S. Physical adsorption of CO_2 in biomass at atmospheric pressure and ambient temperature. *Environ. Chem. Lett.* **2020**, *18*, 1423−1431.

(13) Guo, J.-X.; Shu, S.; Liu, X.-L.; Wang, X.-J.; Yin, H.-Q.; Chu, Y.-H. Influence of Fe loadings on desulfurization performance of activated carbon treated by nitric acid. *Environ. Technol.* **2017**, *38*, 266−276.

(14) Soffian, M. S.; Halim, F. Z. A.; Aziz, F.; Rahman, M. A.; Amin, M. A. M.; Chee, D. N. A. Carbon-based material derived from biomass waste for wastewater treatment. *Environ. Adv.* **2022**, *9*, No. 100259.

(15) Tao, H.-C.; Zhang, H.-R.; Li, J.-B.; Ding, W.-Y. Biomass based activated carbon obtained from sludge and sugarcane bagasse for removing lead ion from wastewater. *Bioresour. Technol.* **2015**, *192*, 611−617.

(16) Tao, L.; Huang, Y.; Yang, X.; Zheng, Y.; Liu, C.; Di, M.; Zheng, Z. Flexible anode materials for lithium-ion batteries derived from waste biomass-based carbon nanofibers: I. Effect of carbonization temperature. *RSC Adv.* **2018**, *8*, 7102−7109.

(17) Hong, K.-l.; Qie, L.; Zeng, R.; Yi, Z.-q.; Zhang, W.; Wang, D.; Yin, W.; Wu, C.; Fan, Q.-j.; Zhang, W.-x.; Huang, Y. h. Biomass derived hard carbon used as a high performance anode material for sodium ion batteries. *J. Mater. Chem. A* **2014**, *2*, 12733−12738.

(18) Dubey, P.; Shrivastav, V.; Maheshwari, P. H.; Sundriyal, S. Recent advances in biomass derived activated carbon electrodes for hybrid electrochemical capacitor applications: Challenges and opportunities. *Carbon* **2020**, *170*, 1.

(19) Wang, T.; Zhai, Y.; Zhu, Y.; Li, C.; Zeng, G. A review of the hydrothermal carbonization of biomass waste for hydrochar formation: Process conditions, fundamentals, and physicochemical properties. *Renewable Sustainable Energy Rev.* **2018**, *90*, 223−247.

(20) Hoekman, S. K.; Broch, A.; Robbins, C. Hydrothermal carbonization (HTC) of lignocellulosic biomass. *Energy Fuels* **2011**, *25*, 1802−1810.

(21) Funke, A.; Ziegler, F. Hydrothermal carbonization of biomass: a summary and discussion of chemical mechanisms for process engineering. *Biofuel, Bioprod. Biorefin.* **2010**, *4*, 160−177.

(22) Xiao, L.-P.; Shi, Z.-J.; Xu, F.; Sun, R.-C. Hydrothermal carbonization of lignocellulosic biomass. *Bioresour. Technol.* **2012**, *118*, 619−623.

(23) Libra, J. A.; Ro, K. S.; Kammann, C.; Funke, A.; Berge, N. D.; Neubauer, Y.; Titirici, M.-M.; Fühner, C.; Bens, O.; Kern, J.; Emmerich, K. H. Hydrothermal carbonization of biomass residuals: a comparative review of the chemistry, processes and applications of wet and dry pyrolysis. *Biofuels* **2011**, *2*, 71−106.

(24) Gupta, D.; Mahajani, S.; Garg, A. Effect of hydrothermal carbonization as pretreatment on energy recovery from food and paper wastes. *Bioresour. Technol.* **2019**, *285*, No. 121329.

(25) Rawat, S.; Mishra, R. K.; Bhaskar, T. Biomass derived functional carbon materials for supercapacitor applications. *Chemosphere* **2022**, *286*, No. 131961.
(26) Shaker, M.; Ghazvini, A. A. S.; Cao, W.; Riahifar, R.; Ge, Q. Biomass-derived porous carbons as supercapacitor electrodes−A review. *New Carbon Mater.* **2021**, *36*, 546−572.
(27) Yang, H.; Tang, Y.; Huang, X.; Wang, L.; Zhang, Q. Activated porous carbon derived from walnut shells with promising material properties for supercapacitors. *J. Mater. Sci.: Mater. Electron.* **2017**, *28*, 18637−18645.
(28) Tian, W.; Gao, Q.; Tan, Y.; Yang, K.; Zhu, L.; Yang, C.; Zhang, H. Bio-inspired beehive-like hierarchical nanoporous carbon derived from bamboo-based industrial by-product as a high performance supercapacitor electrode material. *J. Mater. Chem. A* **2015**, *3*, 5656−5664.
(29) Sundriyal, S.; Shrivastav, V.; Gupta, A.; Shrivastav, V.; Deep, A.; Dhakate, S. R. Pencil peel derived mixed phase activated carbon and metal-organic framework derived cobalt-tungsten oxide for high-performance hybrid supercapacitors. *Mater. Res. Bull.* **2021**, *142*, No. 111396.
(30) Sodtipinta, J.; Ieosakulrat, C.; Poonyayant, N.; Kidkhunthod, P.; Chanlek, N.; Amornsakchai, T.; Pakawatpanurut, P. Interconnected open-channel carbon nanosheets derived from pineapple leaf fiber as a sustainable active material for supercapacitors. *Ind. Crops Prod.* **2017**, *104*, 13−20.
(31) Thubsuang, U.; Laebang, S.; Manmuanpom, N.; Wongkasemjit, S.; Chaisuwan, T. Tuning pore characteristics of porous carbon monoliths prepared from rubber wood waste treated with H_3PO_4 or NaOH and their potential as supercapacitor electrode materials. *J. Mater. Sci.* **2017**, *52*, 6837−6855.
(32) Wang, H.; Li, Z.; Tak, J. K.; Holt, C. M.; Tan, X.; Xu, Z.; Amirkhiz, B. S.; Harfield, D.; Anyia, A.; Stephenson, T.; Mitlin, D. Supercapacitors based on carbons with tuned porosity derived from paper pulp mill sludge biowaste. *Carbon* **2013**, *57*, 317−328.
(33) Ma, G.; Li, J.; Sun, K.; Peng, H.; Feng, E.; Lei, Z. Tea-leaves based nitrogen-doped porous carbons for high-performance supercapacitors electrode. *J. Solid State Electrochem.* **2017**, *21*, 525−535.
(34) Gao, F.; Qu, J.; Zhao, Z.; Wang, Z.; Qiu, J. Nitrogen-doped activated carbon derived from prawn shells for high-performance supercapacitors. *Electrochim. Acta* **2016**, *190*, 1134−1141.
(35) Wahid, M.; Puthusseri, D.; Phase, D.; Ogale, S. Enhanced capacitance retention in a supercapacitor made of carbon from sugarcane bagasse by hydrothermal pretreatment. *Energy Fuel* **2014**, *28*, 4233−4240.
(36) Biswal, M.; Banerjee, A.; Deo, M.; Ogale, S. From dead leaves to high energy density supercapacitors. *Energy Environ. Sci.* **2013**, *6*, 1249−1259.
(37) Chen, M.; Kang, X.; Wumaier, T.; Dou, J.; Gao, B.; Han, Y.; Xu, G.; Liu, Z.; Zhang, L. Preparation of activated carbon from cotton stalk and its application in supercapacitor. *J. Solid State Electrochem.* **2013**, *17*, 1005−1012.
(38) Pal, B.; Yang, S.; Ramesh, S.; Thangadurai, V.; Jose, R. Electrolyte selection for supercapacitive devices: A critical review. *Nanoscale Adv.* **2019**, *1*, 3807−3835.
(39) Pal, B.; Krishnan, S. G.; Vijayan, B. L.; Harilal, M.; Yang, C.-C.; Ezema, F. I.; Yusoff, M. M.; Jose, R. In situ encapsulation of tin oxide and cobalt oxide composite in porous carbon for high-performance energy storage applications. *J. Electroanal. Chem.* **2018**, *817*, 217−225.
(40) Galiński, M.; Lewandowski, A.; Stępniak, I. Ionic liquids as electrolytes. *Electrochim. Acta* **2006**, *51*, 5567−5580.
(41) An, Y.; Tian, Y.; Li, Y.; Wei, C.; Tao, Y.; Liu, Y.; Xi, B.; Xiong, S.; Feng, J.; Qian, Y. Heteroatom-doped 3D porous carbon architectures for highly stable aqueous zinc metal batteries and non-aqueous lithium metal batteries. *Chem. Eng. J.* **2020**, *400*, No. 125843.
(42) Boujibar, O.; Ghosh, A.; Achak, O.; Chafik, T.; Ghamouss, F. A high energy storage supercapacitor based on nanoporous activated carbon electrode made from Argan shells with excellent ion transport in aqueous and non-aqueous electrolytes. *J. Energy Storage* **2019**, *26*, No. 100958.
(43) Yoshizawa, N.; Maruyama, K.; Yamada, Y.; Ishikawa, E.; Kobayashi, M.; Toda, Y.; Shiraishi, M. XRD evaluation of KOH activation process and influence of coal rank. *Fuel* **2002**, *81*, 1717−1722.
(44) Zhao, Y.; Ran, W.; He, J.; Song, Y.; Zhang, C.; Xiong, D.-B.; Gao, F.; Wu, J.; Xia, Y. Oxygen-rich hierarchical porous carbon derived from artemia cyst shells with superior electrochemical performance. *ACS Appl. Mater. Interfaces* **2015**, *7*, 1132−1139.
(45) Chen, T.; Tang, Y.; Qiao, Y.; Liu, Z.; Guo, W.; Song, J.; Mu, S.; Yu, S.; Zhao, Y.; Gao, F. All-solid-state high-performance asymmetric supercapacitors based on novel MnS nanocrystal and activated carbon materials. *Sci. Rep.* **2016**, *6*, No. 23289.
(46) Chen, J.; Zhang, L.; Yang, G.; Wang, Q.; Li, R.; Lucia, L. A. Preparation and characterization of activated carbon from hydrochar by phosphoric acid activation and its adsorption performance in prehydrolysis liquor. *BioResources* **2017**, *12*, 5928−5941.
(47) Thommes, M.; Kaneko, K.; Neimark, A. V.; Olivier, J. P.; Rodriguez-Reinoso, F.; Rouquerol, J.; Sing, K. S. Physisorption of gases, with special reference to the evaluation of surface area and pore size distribution (IUPAC Technical Report). *Pure Appl. Chem.* **2015**, *87*, 1051−1069.
(48) Hu, Z.; Srinivasan, M. P.; Ni, Y. Preparation of mesoporous high-surface-area activated carbon. *Adv. Mater.* **2000**, *12*, 62−65.
(49) Sing, K.; Everett, D.; Haul, R.; Moscou, L.; Pierotti, R.; Rouquerol, J.; Siemieniewska, T. International union of pure and applied chemistry, IUPAC. *Pure Appl. Chem.* **1985**, *57*, 603.
(50) Fu, S.; Fang, Q.; Li, A.; Li, Z.; Han, J.; Dang, X.; Han, W. Accurate characterization of full pore size distribution of tight sandstones by low-temperature nitrogen gas adsorption and high-pressure mercury intrusion combination method. *Energy Sci. Eng.* **2021**, *9*, 80−100.
(51) Li, J.; Zhang, W.; Zhang, X.; Huo, L.; Liang, J.; Wu, L.; Liu, Y.; Gao, J.; Pang, H.; Xue, H. Copolymer derived micro/meso-porous carbon nanofibers with vacancy-type defects for high-performance supercapacitors. *J. Mater. Chem. A* **2020**, *8*, 2463−2471.
(52) Zhao, W.; Luo, L.; Chen, T.; Li, Z.; Zhang, Z.; Wang, H.; Rao, J.; Feo, L.; Fan, M. Synthesis and characterization of Pt-N-doped activated biocarbon composites for hydrogen storage. *Composites, Part B* **2019**, *161*, 464−472.
(53) Huang, K.-J.; Zhang, J.-Z.; Shi, G.-W.; Liu, Y.-M. Hydrothermal synthesis of molybdenum disulfide nanosheets as supercapacitors electrode material. *Electrochim. Acta* **2014**, *132*, 397−403.
(54) Qie, L.; Chen, W.; Xu, H.; Xiong, X.; Jiang, Y.; Zou, F.; Hu, X.; Xin, Y.; Zhang, Z.; Huang, Y. Synthesis of functionalized 3D hierarchical porous carbon for high-performance supercapacitors. *Energy Environ. Sci.* **2013**, *6*, 2497−2504.
(55) Hulicova-Jurcakova, D.; Seredych, M.; Lu, G. Q.; Bandosz, T. J. Combined effect of nitrogen-and oxygen-containing functional groups of microporous activated carbon on its electrochemical performance in supercapacitors. *Adv. Funct. Mater.* **2009**, *19*, 438−447.
(56) Pietrzak, R. XPS study and physico-chemical properties of nitrogen-enriched microporous activated carbon from high volatile bituminous coal. *Fuel* **2009**, *88*, 1871−1877.
(57) Zhang, S.; Wang, L.; Zhang, Y.; Cao, F.; Sun, Q.; Ren, X.; Wennersten, R. Effect of hydroxyl functional groups on SO2 adsorption by activated carbon. *J. Environ. Chem. Eng.* **2022**, *10*, No. 108727.
(58) Zequine, C.; Ranaweera, C.; Wang, Z.; Dvornic, P. R.; Kahol, P.; Singh, S.; Tripathi, P.; Srivastava, O.; Singh, S.; Gupta, B. K.; et al. High-performance flexible supercapacitors obtained via recycled jute: bio-waste to energy storage approach. *Sci. Rep.* **2017**, *7*, No. 1174.
(59) Sun, L.; Zhao, Z.; Sun, Y.; Wang, X.; Liu, X.; Yang, Y.; Qiu, J. Activated coal-based graphene with hierarchical porous structures for ultra-high energy density supercapacitors. *Diamond Relat. Mater.* **2020**, *106*, No. 107827.
(60) Mei, B.-A.; Munteshari, O.; Lau, J.; Dunn, B.; Pilon, L. Physical interpretations of Nyquist plots for EDLC electrodes and devices. *J. Phys. Chem. C* **2018**, *122*, 194−206.

https://doi.org/10.1021/acsomega.2c05887
ACS Omega 2023, 8, 5285−5299

(61) Guo, F.; Jiang, X.; Jia, X.; Liang, S.; Qian, L.; Rao, Z. Synthesis of biomass carbon electrode materials by bimetallic activation for the application in supercapacitors. *J. Electroanal. Chem.* **2019**, *844*, 105−115.
(62) Feng, J.; Zhang, Z.; Li, L.; Yang, J.; Xiong, S.; Qian, Y. Ether-based nonflammable electrolyte for room temperature sodium battery. *J. Power Sources* **2015**, *284*, 222−226.
(63) Oglou, R. C.; Gokce, Y.; Yagmur, E.; Ghobadi, T. G. U.; Aktas, Z. Highly stable Megalopolis lignite based N and S self-doped hierarchically porous activated carbons for high performance supercapacitors and ash content effects on performance. *J. Energy Storage* **2022**, *46*, No. 103817.
(64) Karnan, M.; Subramani, K.; Srividhya, P.; Sathish, M. Electrochemical studies on corncob derived activated porous carbon for supercapacitors application in aqueous and non-aqueous electrolytes. *Electrochim. Acta* **2017**, *228*, 586−596.
(65) Mathis, T. S.; Kurra, N.; Wang, X.; Pinto, D.; Simon, P.; Gogotsi, Y. Energy storage data reporting in perspective—guidelines for interpreting the performance of electrochemical energy storage systems. *Adv. Eng. Mater.* **2019**, *9*, No. 1902007.
(66) da Silveira Firmiano, E. G.; Rabelo, A. C.; Dalmaschio, C. J.; Pinheiro, A. N.; Pereira, E. C.; Schreiner, W. H.; Leite, E. R. Supercapacitor electrodes obtained by directly bonding 2D MoS_2 on reduced graphene oxide. *Adv. Eng. Mater.* **2014**, *4*, No. 1301380.
(67) Ashassi-Sorkhabi, H.; La'le Badakhshan, P.; Asghari, E. Electrodeposition of three dimensional-porous Ni/Ni $(OH)_2$ hierarchical nano composite via etching the Ni/Zn/Ni $(OH)_2$ precursor as a high-performance pseudocapacitor. *Chem. Eng. J.* **2016**, *299*, 282−291.
(68) Huang, G.; Wang, Y.; Zhang, T.; Wu, X.; Cai, J. High-performance hierarchical N-doped porous carbons from hydrothermally carbonized bamboo shoot shells for symmetric supercapacitors. *J. Taiwan Inst. Chem. Eng.* **2019**, *96*, 672−680.
(69) Linares-Solano, A.; Lillo-Ródenas, M.; Marco-Lozar, J. P.; Kunowsky, M.; Romero-Anaya, A. J. NaOH and KOH for preparing activated carbons used in energy and environmental applications. *Int. J. Energy Environ. Econ.* **2012**, *20*, 355.
(70) Olivier, J. P. Improving the models used for calculating the size distribution of micropore volume of activated carbons from adsorption data. *Carbon* **1998**, *36*, 1469−1472.
(71) Liu, T. C.; Pell, W.; Conway, B.; Roberson, S. Behavior of molybdenum nitrides as materials for electrochemical capacitors: comparison with ruthenium oxide. *J. Electrochem. Soc.* **1998**, *145*, 1882.

https://doi.org/10.1021/acsomega.2c05887
ACS Omega 2023, 8, 5285−5299